J Solid State Electrochem (2009) 13:1215–1226
DOI 10.1007/s10008-008-0651-y

ORIGINAL PAPER

Nanoporous oxide formation by anodic oxidation of Nb in sulphate–fluoride electrolytes

Bogdan Tzvetkov · Martin Bojinov · Assen Girginov

Received: 16 June 2008 / Revised: 7 August 2008 / Accepted: 8 August 2008 / Published online: 27 August 2008

Abstract The influence of hydrofluoric acid (HF) concentration and applied potential on the processes of anodic oxidation of Nb in sulphuric acid solution was studied by chronoamperometry, electrochemical impedance spectroscopy and scanning electron microscopy. During the first stage of the process, a compact barrier film is formed. On top of this film, a porous overlayer starts to form, then the nanopores grow into an ordered nanostructure. Subsequently, secondary 3D flower-shaped structures begin to form. These structures gradually spread all over the surface as an irregular multilayer film. The rates of the process of porous overlayer formation and subsequent growth of nanopore arrays increase with applied potential as well as with the HF concentration. The films have been characterised ex situ by electrochemical impedance spectroscopy at open circuit potential and capacitance vs. potential measurements to follow the different stages of nanoporous film formation with electrochemical methods. The impedance spectra and capacitance vs. potential curves have been interpreted using previously proposed models for the amorphous semiconductor/electrolyte interface. An attempt to rationalise the mechanism of nanoporous layer growth is presented by using the conceptual views of the mixed-conduction model and recent ideas for porous film formation on valve metals.

Keywords Niobium · Nanoporous oxide · Scanning electron microscopy · Electrochemical impedance spectroscopy · Capacitance measurements

B. Tzvetkov · M. Bojinov (✉) · A. Girginov
Department of Physical Chemistry,
University of Chemical Technology and Metallurgy,
8 Kl. Ohridski Blvd.,
1756 Sofia, Bulgaria
e-mail: martin@uctm.edu

Introduction

Recently, valve metals have offered promises as cost-effective sources of ordered oxide nanotubes [1–6]. Their major applications, due to the well-developed and easily controllable specific surface, are in the field of catalysis [7, 8], photocatalytic water splitting and gas sensors [9–14]. Specifically, the application of niobium oxide is generally as a catalyst in organic synthesis and promoter/activator to other catalysts (Ru, Rh, Pt, Re, Ni, Cr, W, etc.) [15], as well as in capacitor industry, replacing the rare and more expensive tantalum (http://powerelectronics.com/mag/Ken Yi March 2003.pdf; http://www.nec-tokin.com/english/product/cap/topics/0107_qa.html].

Even though Nb has been demonstrated to form oxide nanotube arrays in acidic media containing small amounts of hydrofluoric acid (HF) [5, 16], quantitative data on the process rate and controlling factors are still scarce. In our previous works [17, 18], the general and local electrochemical behaviour of nanoporous anodic niobium oxide in sulphate solutions with different additions of HF at potentials up to 10 V was studied by means of chronoamperometry, electrochemical impedance spectroscopy (EIS) and local electrochemical impedance spectroscopy (LEIS). As a conclusion, the CPE-like distribution of the high-frequency capacitive time constant observed in the impedance spectra was found to be due to a 2D distribution (owed to the fact that both an ordered crystallisation structure and an array of nanopores are present at the oxide/electrolyte interface) and a 3D distribution, resulting from the profiles of defect-induced conductivity in the bulk oxide owed to the processes of barrier layer growth, Nb dissolution through the barrier layer and subsequent formation of a porous overlayer.

The objective of the present work was to study further the evolution of the nanoporous layer growth process over a

wide range of potentials (20–60 V) and anodic oxidation times (up to 6 h) by means of scanning electron microscopy (SEM) combined with EIS and capacitance vs. potential measurements for the already formed oxides. The impedance and capacitance data are interpreted using previously proposed models of the semiconductor/electrolyte interface, and a tentative mechanism of the formation and growth of the nanoporous oxide overlayer is proposed.

Experimental

Electrodes and electrolytes

The working electrode material was pure Nb (99.9%, Goodfellow) manufactured in the form of rod. The working electrodes were mechanically abraded with emery paper up to grade 2400, followed by polishing with diamond paste up to 0.5 μm, degreasing with acetone and drying with hot air. A conventional electrolytic cell featuring a large area Pt mesh counter electrode and a saturated calomel reference electrode (E=0.242 V vs. the standard hydrogen electrode) was employed. The electrolytes were prepared from reagent grade H_2SO_4 and HF with bidistilled water. The measurements have been performed at room temperature (20±1 °C) in naturally aerated solutions. No insulation of the working electrode was attempted, but instead, a precisely defined portion of the rod was immersed in the electrolyte in order to expose an area of 1 cm^2.

Apparatus and procedure

Current vs. time curves at different potentials (20, 40 and 60 V) were measured by a laboratory-made high-voltage potentiostat/galvanostat connected to a personal computer via an analog-to-digital converter card. Anodic oxidation has been carrier out first at constant current to reach the predefined potential and then potentiostatically for various times ranging from 10 min to 6 h. SEM observations were carried out on a JEOL microscope. Electrochemical impedance spectra at open circuit and capacitance vs. potential sweeps in the negative direction from 1 to −0.5 V with a scan rate of 1 mV s^{-1} have been registered using an Autolab PGSTAT 30 with a FRA module controlled by FRA2 software (Eco Chemie, The Netherlands). The frequency range of the impedance measurements was 0.02 Hz–120 kHz at an ac amplitude of 20 mV(rms). The linearity of the impedance was verified by measuring spectra at different amplitudes between 2 and 20 mV, whereas the causality was determined by a Kramers–Kronig compatibility test. Data that did not pass the test (usually at the low-frequency end) were rejected. All the impedance measurements have been triplicated to ensure reproducibility, which was less than 1% by impedance magnitude and less than 3° by phase angle. The fitting of the data to equivalent circuits was performed using ZView software (Scribner Associates). Capacitance vs. potential data were measured at a fixed frequency of 1 kHz using an ac amplitude of 20 mV(rms). No significant difference in the capacitance values in the frequency range 1–10 kHz was observed in preliminary measurements. For the fitting of the capacitance–potential curves to models proposed in the literature, Origin 7.5 software (OriginLab) was employed.

Results

Chronoamperometry

Figure 1 shows the current vs. time curves of Nb measured in 1 M H_2SO_4+0.25 M HF in the potential range 20 to 60 V. The curves are similar to those reported previously by us and other authors for H_2SO_4 and H_3PO_4 solutions containing HF [5, 16, 18]. They depict the formation of a barrier layer (until the minimum of the curves, about 0.25 h) and the subsequent growth of the nanoporous overlayer (current increase, until about 3 h). A further alteration in the mechanism of the formation process is detected as a decrease in the slope to reach a stable current density (at approximately 5–6 h). No meaningful dependence of the current values on formation potential has been observed, which may mean that the applied potential is consumed mainly in the barrier sublayer and thus does not directly influence the processes of formation of the nanoporous overlayer.

For comparison, current vs. time curves measured in 1 M H_2SO_4 with no HF addition are also presented in Fig. 1. It is worth noting that the current values in general increase with formation potential, which may indicate an increase in the

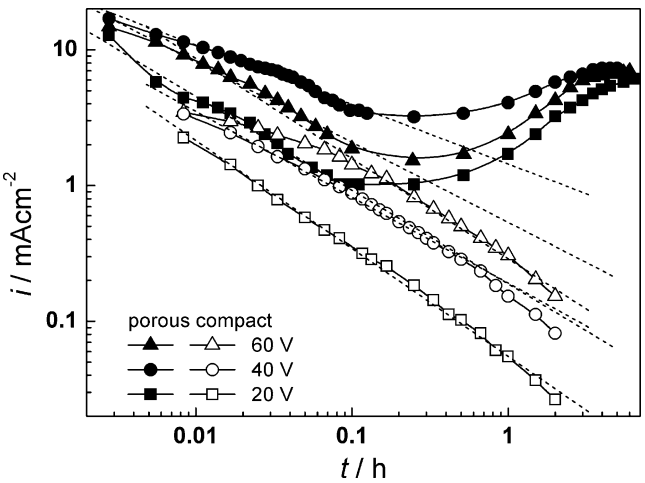

Fig. 1 Current vs. time curves during potentiostatic oxidation of Nb in 1 M H_2SO_4+0.25 M HF (*closed symbols*) and 1 M H_2SO_4 (*open symbols*) at 20, 40 and 60 V. The *dashed lines* are linear fits of the log$i$–log$t$ dependences

electronic current during anodisation at a higher potential [19].The current vs. time curves are qualitatively similar to current vs. time measurements during oxidation of a range of valve metals, i.e. they are linear in a log–log plot with a slope close to −0.8, indicating a high-field mechanism of barrier layer growth [20]. The slopes of the decreasing parts of the curves measured in the presence of HF are comparable, at least for potentials of 20 and 60 V, indicating that the barrier film growth stage proceeds probably by a similar mechanism regardless of the addition of HF that enhances the dissolution of the oxide.

In the following paragraphs, experimental data on the ex situ characterisation of the anodic oxides formed at different points of the current vs. time curves are presented and discussed.

Scanning electron microscopy

Figure 2a shows the niobium sample after pretreatment, bearing the naturally formed oxide layer before anodisation and revealing a smooth surface. As mentioned in the previous section, the anodisation of Nb in sulphuric–hydrofluoric acid media begins with formation of a compact barrier layer within the first 0.25 h (Fig. 2b). Subsequently, the growth of the porous nanostructured overlayer is initiated (the initial rise of the current, Fig. 1) as observed in Fig. 2c. Then, the nanopores grow into columnar nanostructures (Fig. 2d,e) up to about 2 h. At this moment, the process reaches its alteration point and secondary 3D structures begin to form (Fig. 2f). These "flowers" initially spread out all over the surface and then "pile up" into multiple irregular layers, completely covering the surface (Fig. 2g,h). It is noteworthy that the secondary structures, or the so-called flowers, are different formations from the previously reported "cones" [21, 22] (in HF solutions) and "sunflowers" [23] (in H_3PO_4 at potential close to breakdown). It is also important to note that preliminary estimation of the thickness of the nanoporous overlayer by microscopic examination of cross-sections gives values of the order of 300–400 nm, in accordance to reports from other authors [16].

The study of the influence of HF concentration and potential on the rate of the nanoporous layer formation process proved the previously reported correlations [17, 18]. Figure 3 shows the top views of Nb oxidised in 1 M H_2SO_4+0.25 M HF for 2 h at 20, 40 and 60 V, respectively. It is found that the nanopore diameters at 20 V (Fig. 3a) are smaller than at 40 V (Fig. 3b). For a similar oxidation time at 60 V (Fig. 3c), there is a typical view of an oxide layer completely covered with secondary "flower" structures. Thus, even if the current vs. time curves at the three potentials are qualitatively analogous, the rates of the different stages of the process of secondary overlayer formation are clearly influenced by the applied potential.

The relationship between the rate of the porous oxide layer growth and HF concentration in the electrolyte at 40 V is demonstrated in Fig. 4. The micrograph of the oxide film formed in 1 M H_2SO_4+0.1 M HF (Fig. 4a) resembles more the top view for the anodic layer in 1 M H_2SO_4+0.25 M HF for 1 h (Fig. 2a) than that grown in the same electrolyte and potential for 2 h (Fig. 4b). Experiments in 1 M H_2SO_4+ 0.5 M HF demonstrated that the layers formed for time periods over 1 h were already covered with "flowers" bearing a specific shape characteristic for this medium (Fig. 4c).

Summarising, it can be stated that microscopic observation reveal several consecutive stages of anodic oxidation—barrier layer growth, initiation and growth of the nanoporous

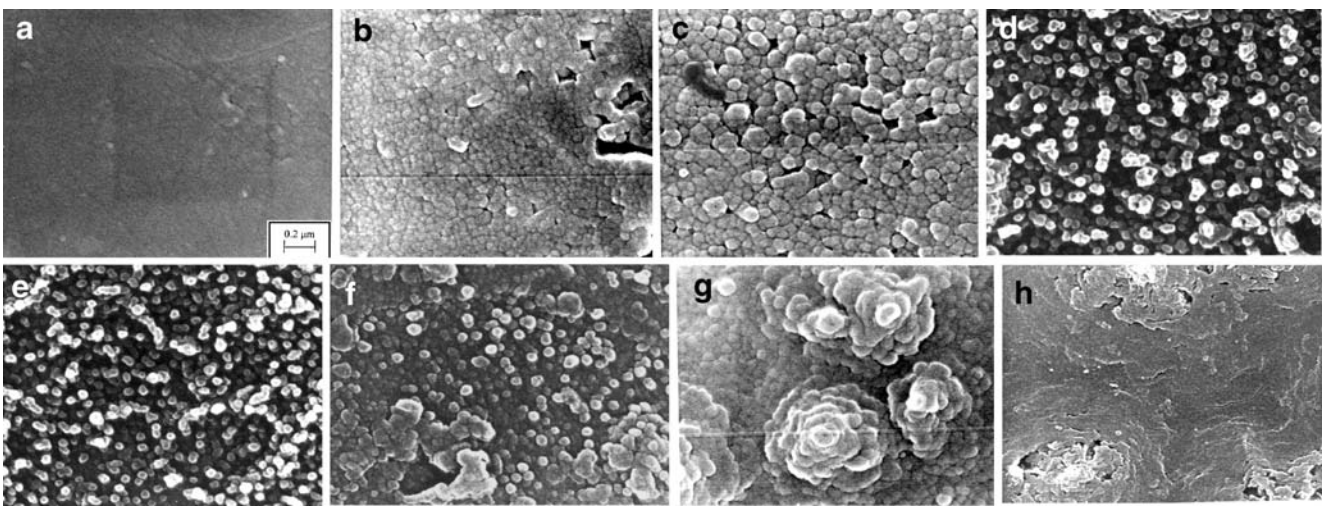

Fig. 2 SEM micrographs of the surface of Nb oxidised at 40 V in 1 M H_2SO_4+0.25 M HF at various times: **a** before anodisation, **b** 0.5 h, **c** 1 h, **d** 1.5 h, **e** 2 h, **f** 2.5 h, **g** 3 h, **h** 5 h. Magnification 5×10^4

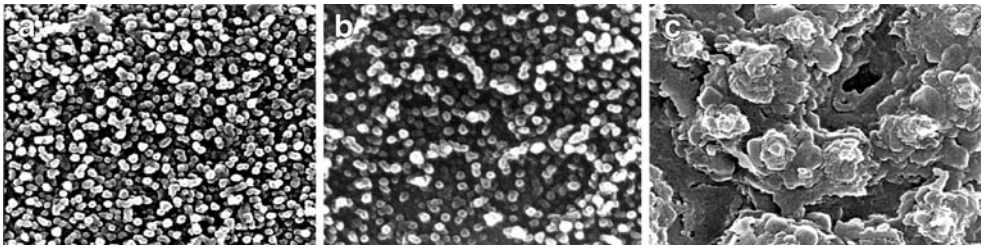

Fig. 3 SEM micrographs of the surface of Nb oxidised for 2 h at: **a** 20, **b** 40 and **c** 60 V in 1 M H_2SO_4+0.25 M HF. Magnification 5×10^4

overlayer and initiation and growth of secondary "flower" structures that completely cover the nanopores. In the next paragraph, the electrical and electrochemical properties of the oxides formed during these reaction stages are characterised by electrochemical impedance spectroscopy.

Electrochemical impedance spectra at open circuit

Electrochemical impedance spectra of the oxides formed during the different reaction stages as identified by SEM were measured in 1 M H_2SO_4 at open circuit conditions. Figure 5 shows the spectra of the oxides formed in 1 M H_2SO_4+ 0.25 M HF at 40 V and oxidation times ranging from 10 min to 5 h. The corresponding spectra of the oxides formed in 1 M H_2SO_4+x M HF (x=0.1, 0.25 and 0.5) at 40 V for different times corresponding to roughly similar surface structures are collected in Fig. 6, whereas the spectra of oxides formed in 1 M H_2SO_4+0.25 M HF for 2 h at applied potentials of 20, 40 and 60 V are shown in Fig. 7. The spectra of oxides formed in otherwise similar conditions but with no HF addition to the electrolyte are summarised in Fig. 8.

The impedance spectra are rather complex and at least three time constants—at very high, intermediate and low frequencies—can be identified in the phase angle vs. frequency curves. The spectra of the films formed in plain 1 M H_2SO_4 solution are qualitatively very similar to those recently reported by Di Quarto et al. [24, 25] for Nb oxidised in 0.5 M H_2SO_4 at potentials up to 5 V. In these papers, the general equivalent circuit for semiconductor/electrolyte interface proposed by Gomes and Vanmaekelbergh [26] that accounts for the impedance behaviour of this interface in the presence of electron transfer and/or recombination via surface states was employed. It was modified to incorporate the theory of amorphous semiconductor/electrolyte interface [27] adapted to anodic oxides by Di Quarto et al. [28]. The circuit is shown in Fig. 9 and has been found to reproduce adequately all the spectra presented in Figs. 5, 6, 7 and 8 (the adequacy of this analog is demonstrated in the figures with solid lines). In the circuit, R_{el} is the uncompensated electrolyte resistance, C_{dl} is the double-layer capacitance at the barrier sublayer/electrolyte interface at the bottom of pores, R_{ct} is the charge transfer resistance at that interface, C_{sc} and R_{sc} are the capacitance and resistance of the amorphous semiconductor/electrolyte interface, C_{ss} and R_{ss} represent the capacitance of the surface states and the resistance of the recombination reaction via these states. On the other hand, the CPE is thought to account for the presence of a continuous distribution in energy of electronic states at the surface of the semiconductor [24].

The dependences of the main relevant circuit parameters—C_{sc}, C_{ss}, R_{sc}, R_{ss} and R_{ct}—on time of oxidation, concentration of added HF and applied potential are collected in Fig. 10 (for the nanoporous oxide) and Fig. 11 (for the barrier-type oxide formed in the absence of HF). It is worth noting that the double-layer capacitance at the barrier sublayer/electrolyte interface C_{dl} was found to preserve quasi-constant values of 100±15 μF cm^{-2} in the case of the nanoporous oxides and 15±2 μF cm^{-2} in the case of the barrier oxides, respectively. This latter value was found to be in good agreement with the calculations of Di Quarto et al. [24] for barrier films formed at potentials up to 5 V.

The following conclusions can be drawn from the evolution of the equivalent circuit parameters with the anodisation conditions:

During both the barrier film growth and the initiation of the nanoporous overlayer formation (up to 1 h of oxidation), both C_{sc} and C_{ss} decrease with time at constant potential, whereas R_{sc} increases (Fig. 10a,b). Such a behaviour can be associated with an increase in the

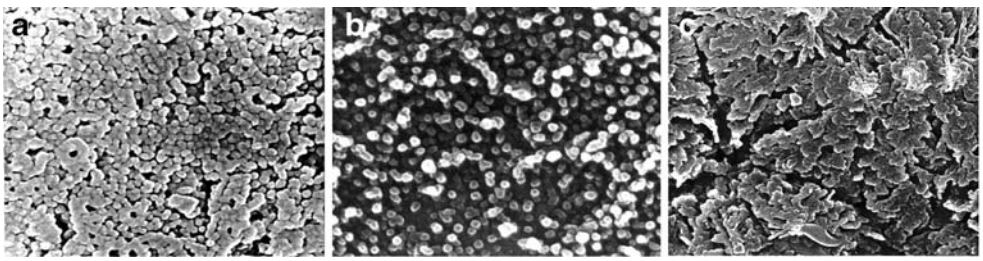

Fig. 4 SEM micrographs of the surface of Nb oxidised for 2 h at 40 V in 1 M H_2SO_4 + **a** 0.1 M, **b** 0.25 M and **c** 0.5 M HF. Magnification 5×10^4

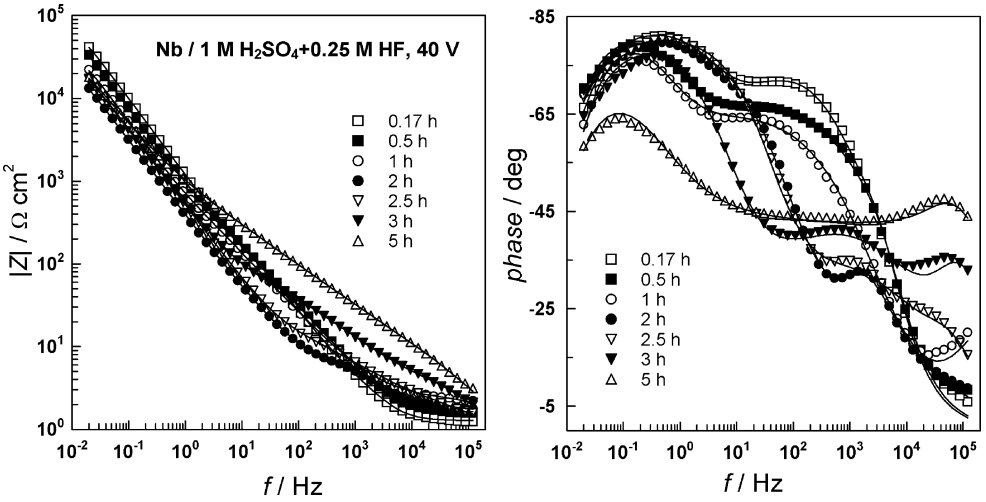

Fig. 5 Electrochemical impedance spectra of Nb oxidised in 1 M H_2SO_4+0.25 M HF at 40 V and various times. Spectra were measured in 1 M H_2SO_4 at open circuit. *Points*: experimental values, *lines*: best-fit calculation according to the adopted equivalent circuit

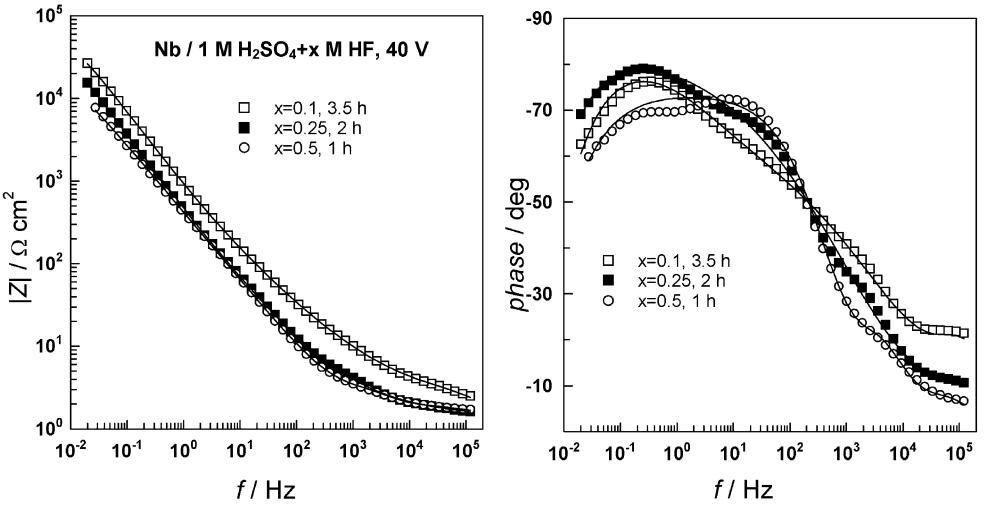

Fig. 6 Electrochemical impedance spectra of Nb oxidised in 1 M H_2SO_4+x M HF (x=0.1, 0.25 and 0.5) at 40 V and various times. Spectra were measured in 1 M H_2SO_4 at open circuit. *Points*: experimental values, *lines*: best-fit calculation according to the adopted equivalent circuit

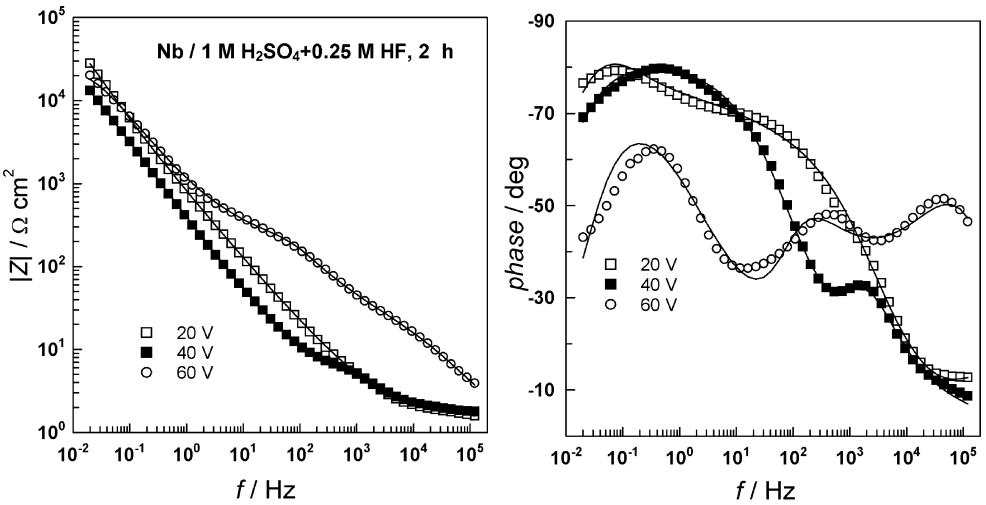

Fig. 7 Electrochemical impedance spectra of Nb oxidised in 1 M H_2SO_4+0.25 M HF for 2 h at 20, 40 and 60 V. Spectra were measured in 1 M H_2SO_4 at open circuit. *Points*: experimental values, *lines*: best-fit calculation according to the adopted equivalent circuit

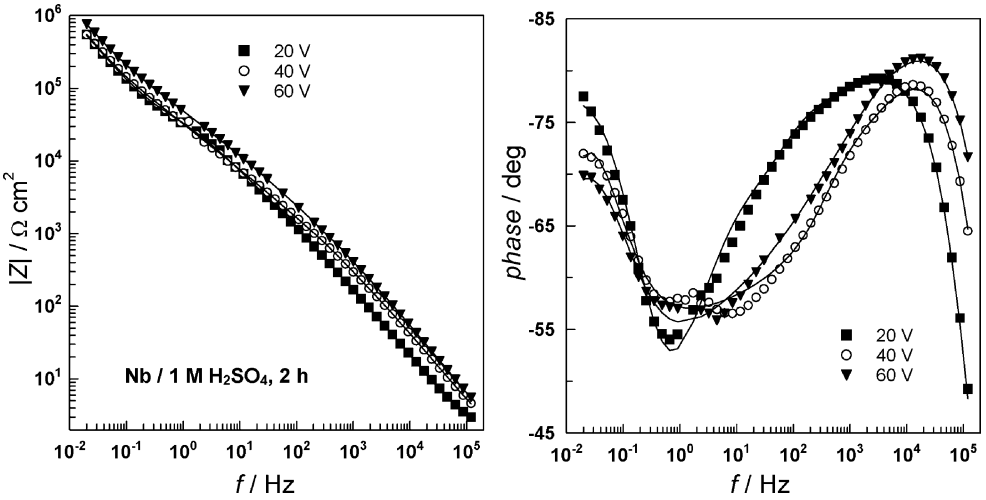

Fig. 8 Electrochemical impedance spectra of Nb oxidised in 1 M H_2SO_4 for 2 h at 20, 40 and 60 V. Spectra were measured in 1 M H_2SO_4 at open circuit. *Points*: experimental values, *lines*: best-fit calculation according to the adopted equivalent circuit

depletion layer width or, in other words, a decrease of the effective donor density in the semiconductor layer. In the subsequent period, there is an increase of both C_{sc} and C_{ss} with time associated with the corresponding decrease in R_{sc}, indicating that the depletion layer width decrease or equivalently the density of donors increases. These features seem to be related to the process of growth of the nanoporous overlayer. A maximum in C_{sc} and C_{ss} and a corresponding minimum in R_{sc} are reached roughly at the time at which the secondary "flower" structures start to spread over the nanopore layer, finally blocking the surface and leading to a further decrease in C_{sc} and C_{ss}, as well as an increase in R_{sc}. Thus, the electrical properties of the semiconductor layer seem to be intimately related to the processes of formation of the ordered nanostructure and its subsequent coverage by the secondary layer, as evidenced by SEM observations. The parameters C_{sc} and C_{ss} tend to increase with the concentration of added HF, whereas an opposite trend is observed for the values of R_{sc} and R_{ct} (Fig. 10c, d). This points to an increased defectiveness of the semiconductor layer formed in the presence of high HF concentrations, which can be traced to the increase of the dissolution rate of the oxide on Nb with HF addition, as demonstrated also earlier [29, 30].

On the other hand, both C_{sc} and C_{ss} decrease with increasing film formation potential, both for the nanoporous (Fig. 10e) and barrier layers (Fig. 11a). This trend can be related to a decrease in the donor concentration and/or increase of the depletion layer width. The decrease in R_{ct} with formation potential can once more be related to the increasing importance of the current carried out by electronic carriers in the oxide when it is formed at higher potentials [19]. The values of R_{sc} and R_{ct} for the nanoporous oxide are approximately 2 orders of magnitude smaller than those for the barrier oxide, which may point out to a much larger conductivity of the nanoporous layer when compared to the barrier film. Such a possibility has been already discussed by Munoz et al. [31, 32] in connection to nanotube overlayers on titanium.

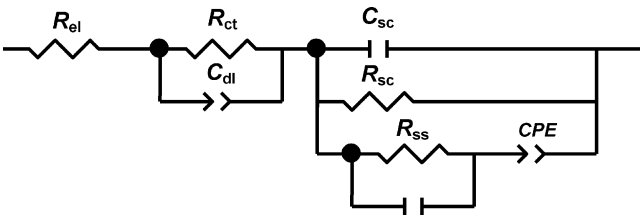

Fig. 9 Equivalent circuit used to interpret the open-circuit impedance measurements. For an explanation of the symbols, see text

Capacitance vs. potential measurements

In order to gain a further insight into the electronic properties of the oxide during the formation of the nanoporous overlayer, capacitance vs. potential curves after oxidation of Nb in conditions similar to those explored above have been registered. Although the authors are perfectly aware of the limitations in interpretation of such measurements, as discussed very recently, e.g. in [33], there are a number of works on Nb that make a successful use of such measurements interpreted within the frames of the amorphous semiconductor–electrolyte interface theory [24, 25, 28, 34].

Capacitance vs. potential curves for Nb oxidised in conditions identical to those for the registration of electrochemical impedance spectra at open circuit are presented in Figs. 12 and 13. As demonstrated in the figures by solid lines, these dependences are successfully described by the low band bending approximation of the amorphous semiconductor theory, according to the equation [24, 25]

$$C^{-1} = \frac{\left(1 + \ln \frac{\psi_S}{\psi_C}\right)^2}{\varepsilon \varepsilon_0 e^2 N} \quad (1)$$

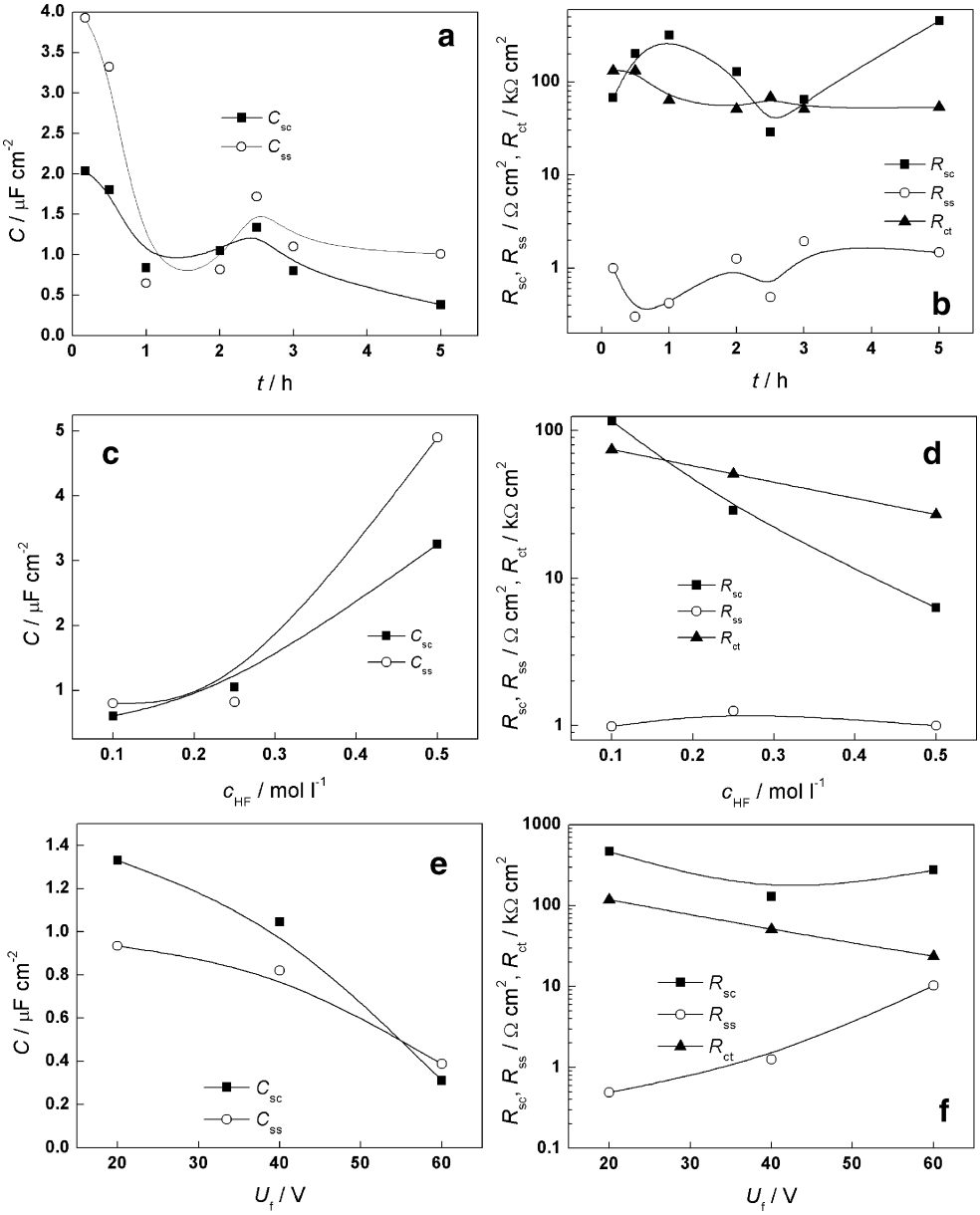

Fig. 10 Dependences of the main equivalent circuit parameters on oxidation time, formation potential and HF concentration for Nb oxidised in 1 M H_2SO_4 with the addition of HF

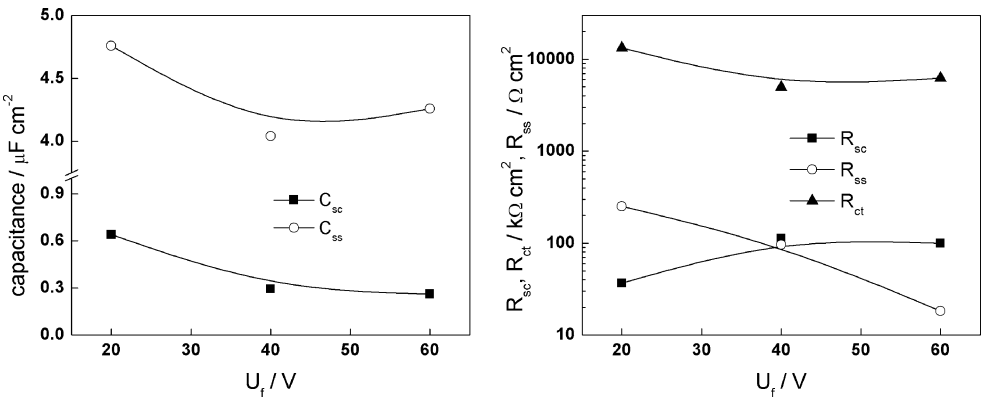

Fig. 11 Dependences of the main equivalent circuit parameters on formation potential and for Nb oxidised in 1 M H_2SO_4 for 2 h

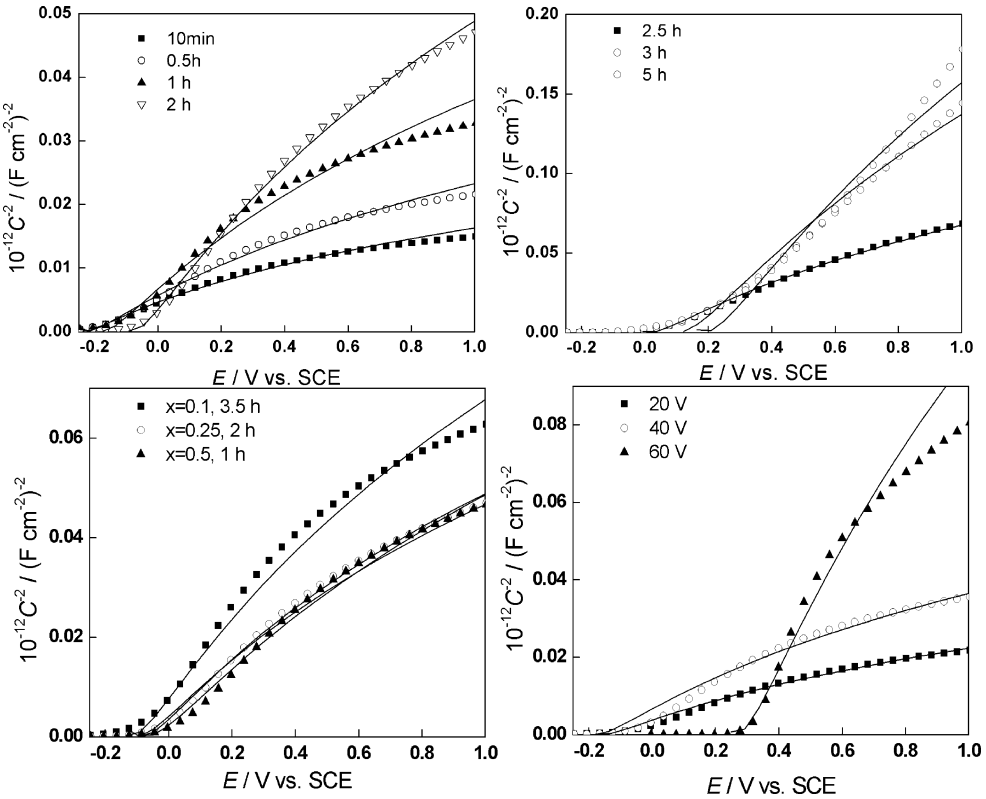

Fig. 12 Capacitance vs. potential curves for Nb oxidised in 1 M H_2SO_4+x M HF (x=0.1, 0.25 and 0.5) at various times and formation potentials. *Points*: experimental data, *lines*: best-fit calculation according to the amorphous semiconductor–electrolyte interface model

where ε=42 for the anodic oxide on Nb [24, 25, 28], ε_0= 8.85×10^{-14} F cm^{-1} is the permittivity of vacuum, e=1.6×10^{-19} C is the charge of the electron, N is the density of states, $\psi_S = E - E_{fb}$ is the band bending, E_{fb} is the flatband potential and ψ_C is the maximum band bending at which the states still respond to the ac signal. The corresponding parameters calculated from the fit of the experimental data to the above equation, namely, N, E_{fb} and ψ_C, are plotted in Fig. 14 as depending on the experimental conditions.

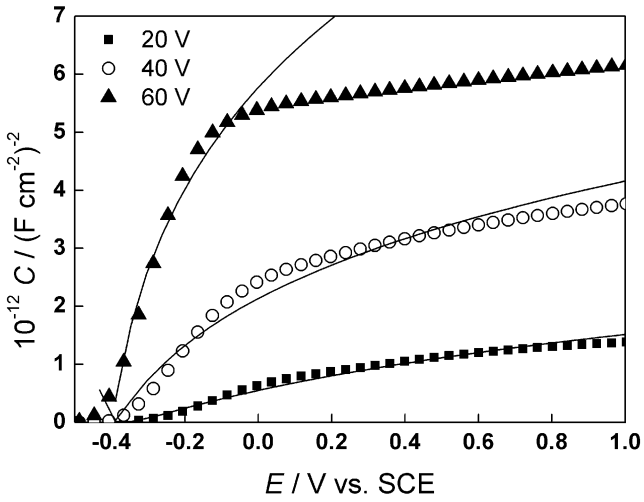

Fig. 13 Capacitance vs. potential curves for Nb oxidised in 1 M H_2SO_4 at various formation potentials. *Points*: experimental data, *lines*: best-fit calculation according to the amorphous semiconductor–electrolyte interface model

The following conclusions can be drawn from the parameter values:

The density of states, N, for the nanoporous oxide decreases with time of oxidation at constant potential (Fig. 14a), which is in broad agreement with the decrease in C_{sc} and C_{ss} (cf. Fig. 10a). The decrease is rather steep during the barrier layer formation and the initiation period of overlayer growth (up to 1 h of oxidation) and is considerably slowed down thereafter during the period of spreading of the nanoporous layer (1–2.5 h). Another steeper decrease is associated with the coverage of the surface with the secondary "flower" structures. The density of states increases with the concentration of added HF (Fig. 14c), indicating once more the increased defectiveness of the semiconductor layer at higher concentrations of the aggressive species leading to an enhanced dissolution process. The density of states in general decreases with formation potential, i.e. oxide film thickness [28, 35] (Fig. 14e), which is also in agreement with the conclusion drawn from the dependences of C_{sc} and C_{ss} with potential (cf. Fig. 10e). The density of states of the porous oxide is approximately 2 orders of magnitude larger than that of a

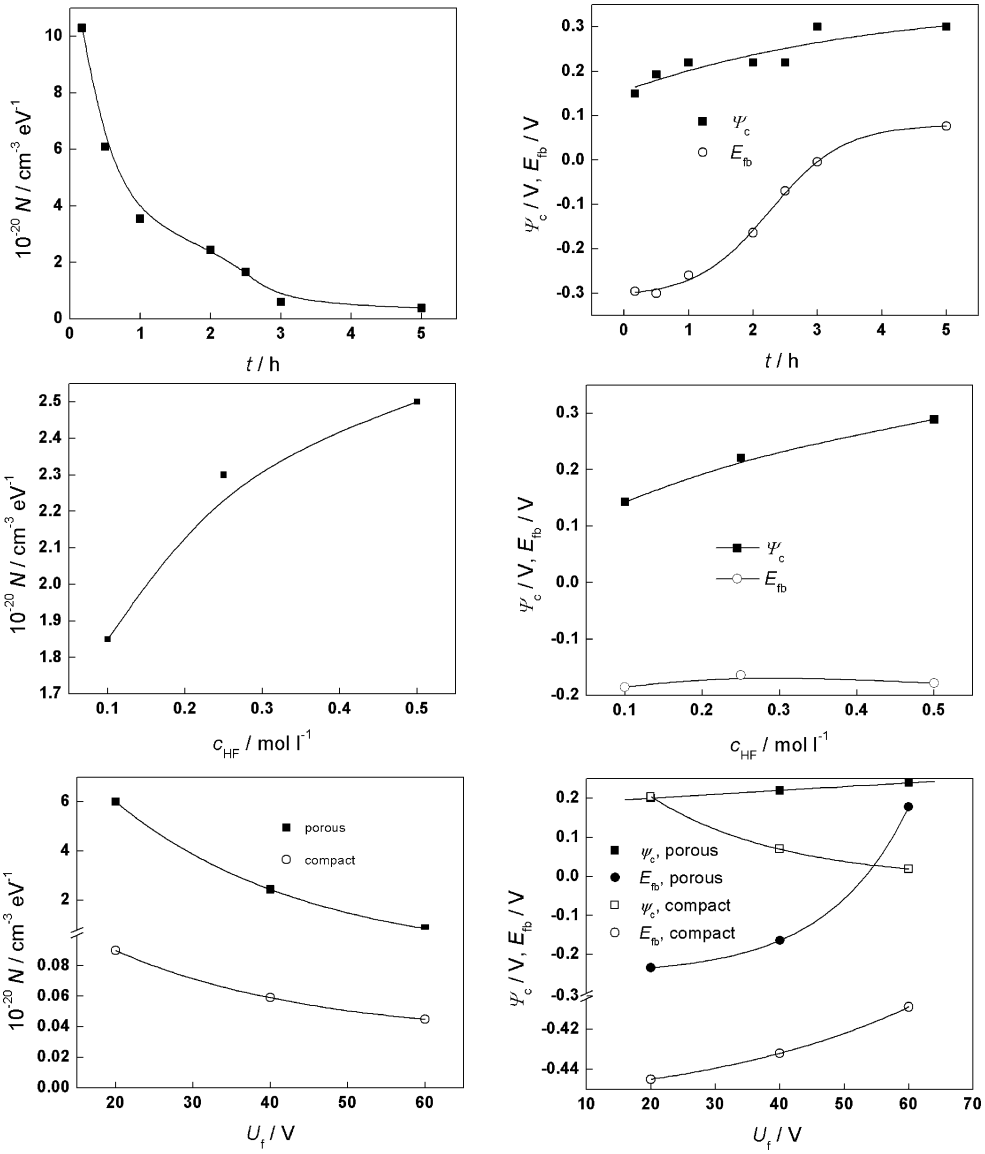

Fig. 14 Parameters of the amorphous semiconductor/electrolyte junction model for Nb oxidised in 1 M H_2SO_4+x M HF (x=0, 0.1, 0.25 and 0.5) at various times and formation potentials

compact oxide formed at the same potential (Fig. 14e), which may once again be traced to the supposedly much higher conductivity of the nanoporous overlayer in comparison to the barrier sublayer, as discussed by other authors in the case of Ti [31, 32]. However, for Ti, it was found that the ratio between the density of states for the nanoporous and compact oxide is around 3, i.e. much smaller part of the nanotubes responds to the perturbation in comparison to the nanoporous layer on Nb which has a more pronounced semiconductor character.

The values of the parameters E_{fb} and ψ_C that characterise the energetics of the junction in the case of the nanoporous oxide are in broad agreement with what has been reported by others for nanotube oxide layers grown on Ti [31, 32]. Namely, the flatband potential for nanoporous layers is more positive than that for a compact film, and also the ψ_C values for the nanotube oxides are larger. In addition, there is an increase in ψ_C with nanotube length (i.e. overall layer thickness) [31], whereas for the compact oxide, ψ_C decreases with applied potential (or film thickness), as reported also by others [28, 34]. The increase of the flatband potential for the nanoporous layer in comparison to the compact film can be interpreted by the introduction of the pore walls having higher donor concentration, which will result in a shift of the energy levels of the barrier layer towards higher energies [31].

Summarising, the electrochemical measurements point to the formation of a dual structure, with a barrier film as an underlayer and a nanoporous overlayer with considerably higher defectiveness. The spreading of the secondary

structures over this layer seems to decrease that defectiveness, most probably by decreasing the active area of the nanostructures that are in contact with the electrolyte solution. In the following chapter, a tentative mechanism of the process of transformation of the barrier film into such a duplex layer is put forward.

Discussion

Very recently, Raja et al. [36] have presented a view to the mechanism of the oxide nanotube growth on Ti in which the regularity of the pore formation is ascribed to the perturbation of the surface strain energy which favours homogeneous F^- adsorption on the film surface. According to this approach, the process has been divided into the following stages: (1) formation of a compact barrier film; (2) thickening of that film and subsequent microfissuring, normally referred as formation of 'easy paths'; (3) secondary porous oxide nucleation through these 'easy paths', subject to perturbation in the balance between the surface energy acting as a stabilising force and the increase in strain energy due to electrostriction, electrostatic and recrystallisation stresses trying to destabilise the surface; (4) coverage of the pore sublayer over the entire surface and growth into nanotubes; (5) pore separation to form individual, self-ordered nanotubes. The dissolution process has been supposed to produce oxygen vacancies which accumulate into the nanotube walls and, as defects with similar sign, they repel each other to acquire regular distribution until they reach a point of saturation when a separation of the walls takes place.

On the other hand, Yasuda et al. [37] have proposed that the initiation of the pores is owed to micro-breakdowns resulting from the layer dissolution and the near-breakdown electric field strength in such oxides, as postulated in the point defect model (PDM) for oxide films [38, 39]. Additionally, a pH gradient is postulated to be established between pore top and bottom, which enables the autocatalytic increase of the dissolution process at the bottom. Subsequently, an ordered linear shape is supposed to be obtained from the wormlike structure due to the larger oxidation area available around the deeper pores which grow to the detriment of the small ones.

According to the PDM [38, 39] and the mixed-conduction model (MCM) [17, 30, 40], the processes of the barrier film growth are described by the following equations:

Film growth and dissolution:

$$M/F : 2\mathrm{Nb_m} \rightarrow 2\mathrm{Nb_{Nb}} + 5V_O^{\cdot\cdot} + 10e_\mathrm{m}^- \quad (2)$$

$$\mathrm{F/S} : 5V_O^{\cdot\cdot} + 5\mathrm{H_2O} \rightarrow 5\mathrm{O_O} + 10\mathrm{H}^+ \quad (3)$$

$$\mathrm{Nb_2O_5} + 10\mathrm{H}^+ + 12\mathrm{F}^- \longrightarrow 2\mathrm{NbF_6^-} + 5\mathrm{H_2O} \quad (4)$$

Niobium dissolution through the film:

$$\mathrm{F}/S : \mathrm{Nb_{Nb}} + 6\mathrm{F}^- \rightarrow V_\mathrm{Nb}^{5'} + \mathrm{NbF_6^-} \quad (5)$$

$$M/F : \mathrm{Nb_m} + V_\mathrm{Nb}^{5'} \rightarrow \mathrm{Nb_{Nb}} + 5e_\mathrm{m}^-. \quad (6)$$

The transport of the oxygen vacancies (with a flux of J_O) supports the film growth. Niobium atoms from the underlying metal (Nb_m) move into the film producing oxygen vacancies, which migrate to the film/solution interface where they interact with the water molecules to form oxygen positions (O_O). Barrier film growth is balanced by dissolution (reaction 4) to achieve a constant thickness of this layer at a given potential. On the other hand, niobium dissolution through the film proceeds by the transport of cation vacancies (J_M). Niobium in niobium position (Nb_{Nb}) at the film/solution interface dissolves generating a niobium vacancy. The vacancy in turn migrates to the metal/film interface where it submerges into the underlying metal restoring the niobium position in the oxide.

Combining these processes with the ideas of Raja et al. [36] for the perturbation of surface tension which favours film

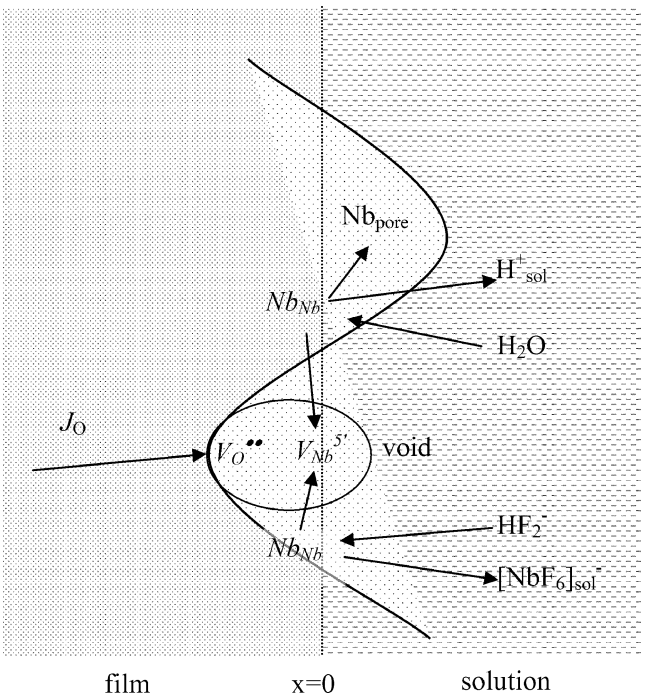

Fig. 15 Schematic of the pore formation during the Nb anodisation

dissolution, we could speculate that at the film/solution interface, the surface is divided into two types: zones of dissolution and zones of growth, as the perturbation of the surface stress is supposed to be regular. We suggest that there are two reactions competing for the zones of growth—Eq. 3 and the following equation:

$$2Nb_{Nb} + 5H_2O \rightarrow Nb_2O_{5,pore} + 2V_{Nb}^{5'} + 10H^+ \quad (7)$$

where $(Nb_2O_5)_{pore}$ is the niobium oxide in the pore walls.

According to Cattarin et al. [29], in high acid media (pH<3) as necessary for niobium oxide dissolution, the fluoride anions are mainly in the form of HF_2^-. The latter interact with niobium atoms at the surface to form a stable soluble complex ($[NbF_6]^-_{sol}$) and generate niobium vacancy, as described by reaction 5.

It is obvious from the schematic shown in Fig. 15 that it is less probable that the oxygen vacancies reach the top of the pore walls (Eq. 3, growing areas) than the bottom of the holes, so the growth could proceed preferably by 7. Thus, both oxygen and niobium vacancies take part in the film formation and dissolution processes at the film surface. As the ionic conduction in anodic layers on Nb is owed rather to J_O than to J_M [41], the increased amount of the $V_{Nb}^{5'}$ generated during metal dissolution will be accumulated at the film/solution interface, forming a negative surface charge which attracts the oxygen vacancies.

These two types of defects could combine with each other. There are two possible reactions for this process:

$$V_O^{\bullet\bullet} + V_{Nb}^{5'} \rightarrow \text{Null} \quad (8)$$

$$V_O^{\bullet\bullet} + V_{Nb}^{5'} \rightarrow \left[V_O^{\cdot\cdot} V_{Nb}^{5'}\right] \quad (9)$$

where Null represents the perfect lattice and $\left[V_O^{\cdot\cdot} V_{Nb}^{5'}\right]$ is a vacancy pair [39].

The first reaction represents the recombination of the two types of vacancies to leave ideal lattice. This reaction has been introduced to reproduce the steady-state and impedance response of Nb in sulphate–fluoride electrolytes at low potentials (up to 5 V) [30] using a combination of the surface charge approach proposed by one of us [42] and a multistep dissolution scheme of Nb at the film/solution interface.

The second possible option is that the two types of vacancies are combined in an empty pair, which we could visualise as a void, i.e. a local recess of the layer at its interface with the electrolyte. This is a viable explanation of how the pores initiate and grow into the barrier layer.

If we include in this picture the surface stress perturbation to define the zones of vacancy recombination into voids (9) in a regular manner, organised pore arrays can form as a result of pore nucleation. Subsequently, the mechanism of pore growth into nanotubes of Yasuda et al. [37] could be well applicable. Within the frames of this mechanism, pore growth initially proceeds in a wormlike manner, establishing a pH gradient between the top and the bottom of the pore. In the next step, a natural selective mechanism owed to the greater oxidation area around the deeper pores helps the self-organisation process to form well-ordered nanostructures. The accumulation of vacancies and/or vacancy pairs at the opposite walls of a nanotube could lead to an increase of the electronic conductivity of the nanotube array due to the fact that these point defects can act as donors or acceptors of electrons, as proposed within the frames of both PDM and MCM [38–40]. Proofs for the increased defectiveness of the nanoporous oxide with respect to a compact film formed in a solution with no HF addition have been found in the electrochemical characterisation results reported in the previous chapter.

The dissolution process, however, continues as the oxidation progresses, and saturation could be reached at the top of the pores so that secondary "flower" structures are spreading all over the surface. The nature of this reaction is most probably chemical, and it may be hypothesised that it is due to supersaturation followed by precipitation at the top of the nanopores. Regardless of its exact mechanism, the process of formation of the secondary structures most probably leads to a decrease in the active area of the nanopores in contact with the electrolyte. This decrease, in turn, tends to diminish the overall defectiveness of the oxide, in agreement with the ex situ electrochemical impedance spectra and capacitance vs. potential curves after oxidation in this region.

Conclusions

The processes of anodic oxidation of niobium in sulphuric acid–hydrofluoric acid solutions have been studied by means of chronoamperometric measurements combined with ex situ microscopic and electrochemical characterisation of the formed oxides. These methods reveal three stages of the film growth in the studied system: (1) formation of a compact barrier film, a process quantitatively described earlier by means of the surface charge approach and involving a reaction of recombination of oppositely charged point defects; (2) further accumulation of vacancy pairs to form voids at particular sites on the surface, as determined by the perturbation of the surface tension, and regular growth of pores into ordered nanostructures; (3) after some point of "saturation" at the top of the nanopores, formation of secondary structures, resembling flowers, which spread all over the surface and then form an irregular multilayer. A qualitative picture of a possible mechanism of stages 2 and 3 based on the concepts of interaction of point defects, localised dissolution and film growth, as well as

surface stress/strain distributions has been proposed and is found to be indirectly supported by the presented experimental results.

Concerning the electrical and electrochemical properties of such layers, they can be best described as a combination of two semiconductor parts, namely, a barrier layer with a relatively small density of states covered by a nanoporous overlayer with a much larger density of states, and hence, much higher conductivity. In that respect, such a structure can be considered as a promising alternative to chemically deposited niobium oxides with prospective applications in the sensor and catalytic industries.

Acknowledgement The funding of this work by the National Science Fund, Bulgarian Ministry of Education and Science, under contract BYX-307/2007 is gratefully acknowledged.

References

1. Yasuda K, Schmuki P (2007) Electrochim Acta 52:4053. doi:10.1016/j.electacta.2006.11.023
2. Macak JM, Schmidt-Stein F, Schmuki P (2007) Electrochem Commun 9:1783. doi:10.1016/j.elecom.2007.04.002
3. Bocchetta P, Conciauro F, Di Quarto F (2007) J Solid State Electrochem 11:1253. doi:10.1007/s10008-007-0280-x
4. Garcia-Vergara SJ, Skeldon P, Thompson GE, Habazaki H (2006) Electrochim Acta 52:681. doi:10.1016/j.electacta.2006.05.054
5. Choi J, Lim J, Lee S, Chang J, Kim K, Cho M (2006) Electrochim Acta 51:5502. doi:10.1016/j.electacta.2006.02.024
6. Rho S, Jahng D, Lim JH, Choi J, Chang J, Lee S et al (2008) Biosens Bioelectron 23:852. doi:10.1016/j.bios.2007.09.001
7. Hutchings G, Taylor S (1999) Catal Today 49:105. doi:10.1016/S0920-5861(98)00414-3
8. Barczuk P, Tsuchiya H, Macak J, Schmuki P, Szymanska D, Makowski O et al (2006) Electrochem Solid-State Lett 9:E13. doi:10.1149/1.2190597
9. Varghese O, Gong D, Paulose M, Ong K, Dickey E, Grimes C (2003) Adv Mat Commun 15:624. doi:10.1002/adma.200304586
10. Varghese O, Gong D, Paulose M, Ong K, Dickey E, Ong K et al (2003) Sensors Actuators B 93:338. doi:10.1016/S0925-4005(03)00222-3
11. Varghese O, Grimes C (2003) J Nanosci Nanotechnol 3:277. doi:10.1166/jnn.2003.158
12. Dickey E, Verghese O, Ong K, Gong D, Paulose M, Grimes C (2002) Sensors 2:91
13. Zuruzi A, Kalmakov A, MacDonald N, Moskovits M (2006) Appl Phys Lett 88:102904. doi:10.1063/1.2185247
14. Mor G, Carvalho M, Varghese O, Pishko M, Grimes C (2004) J Mater Res 19:628. doi:10.1557/jmr.2004.19.2.628
15. Nowak ZM (1999) Chem Rev 99:3603. doi:10.1021/cr9800208
16. Sieber I, Hildebrand H, Friedrich A, Schmuki P (2005) Electrochem Commun 7:97. doi:10.1016/j.elecom.2004.11.012
17. Tzvetkov B, Bojinov M, Girginov A (2006) In: Balabanova E, Dragieva I (eds) Nanoscience & nanotechnology 6. pp 86–90
18. Tzvetkov B, Bojinov M, Girginov A, Pébère N (2007) Electrochim Acta 52:7724. doi:10.1016/j.electacta.2006.12.034
19. Di Quarto F, Piazza S, Sunseri C (1990) Corros Sci 31:267. doi:10.1016/0010-938X(90)90118-O
20. Burstein GT, Davenport AJ (1989) J Electrochem Soc 136:936. doi:10.1149/1.2096890
21. Karlinsey R (2005) Electrochem Commun 7:1190. doi:10.1016/j.elecom.2005.08.027
22. Zhao J, Wang X, Xu R, Mi Y, Lia Y (2007) Electrochem Solid-State Lett 10:C31. doi:10.1149/1.2458528
23. Nagahara K, Sakairi M, Takahashi H, Matsumoto K, Takayama K, Oda Y (2007) Electrochim Acta 52:2134. doi:10.1016/j.electacta.2006.08.030
24. Di Quarto F, La Mantia F, Santamaria M (2005) Electrochim Acta 50:5090. doi:10.1016/j.electacta.2005.03.065
25. Di Quarto F, La Mantia F, Santamaria M (2007) Corros Sci 49:186. doi:10.1016/j.corsci.2006.05.019
26. Gomes WP, Vanmaekelbergh D (1996) Electrochim Acta 41:967. doi:10.1016/0013-4686(95)00427-0
27. Cohen JD, Lang DV (1982) Phys Rev B 25:5321. doi:10.1103/PhysRevB.25.5321
28. Di Quarto F, Piazza S, Sunseri C (1990) Electrochim Acta 35:99. doi:10.1016/0013-4686(90)85045-O
29. Cattarin S, Musiani M, Tribollet B (2002) J Electrochem Soc 149:B457. doi:10.1149/1.1502690
30. Bojinov M, Cattarin S, Musiani M, Tribollet B (2003) Electrochim Acta 48:4107. doi:10.1016/S0013-4686(03)00578-4
31. Munoz AG (2007) Electrochim Acta 52:4167. doi:10.1016/j.electacta.2006.11.035
32. Munoz AG, Chen Q, Schmuki P (2007) J Solid State Electrochem 11:1077. doi:10.1007/s10008-006-0241-9
33. Taveira L, Sagues AA, Macak JM, Schmuki P (2008) J Electrochem Soc 155:C293. doi:10.1149/1.2898503
34. Munoz AG, Staikov G (2006) J Solid State Electrochem 10:329. doi:10.1007/s10008-005-0090-y
35. Modestov AD, Davydov AD (1999) J Electroanal Chem 460:214. doi:10.1016/S0022-0728(98)00378-7
36. Raja KS, Misra M, Paramguru K (2005) Electrochim Acta 51:154. doi:10.1016/j.electacta.2005.04.011
37. Yasuda K, Macak J, Berger S, Ghicov A, Schmuki P (2007) J Electrochem Soc 154:C472. doi:10.1149/1.2749091
38. Chao C, Lin L, Macdonald D (1981) J Electrochem Soc 128:1187. doi:10.1149/1.2127591
39. Macdonald DD (1992) J Electrochem Soc 139:3434. doi:10.1149/1.2069096
40. Bojinov M, Fabricius G, Kinnunen P, Laitinen T, Makela K, Saario T et al (2001) J Electroanal Chem 504:29. doi:10.1016/S0022-0728(01)00423-5
41. Wang M, Hebert K (1999) J Electrochem Soc 146:3741. doi:10.1149/1.1392543
42. Bojinov M (1997) Electrochim Acta 42:3489. doi:10.1016/S0013-4686(97)00037-6